Extremely Low-Profile Periodic 2-D Leaky-Wave Antenna: An Optimal Solution for Antenna-Frontend Integration

Amirhossein Askarian, *Graduate Student Member, IEEE*, Jianping Yao, *Fellow, IEEE*, Zhenguo Lu, *Member, IEEE*, and Ke Wu, *Fellow, IEEE*

Abstract—We investigate and present a very low-profile, high-efficiency, and high-gain 2-D leaky-wave antenna (2DLWA) implemented on a high permittivity substrate operating in the millimeter-wave range, paving the way for the seamless integration of a high-gain and high-efficiency antenna with a frontend. In contrast to the typical air-filled 2DLWA, where a perturbation of the first higher-order mode (TE_1/TM_1) results in highly directed broadside radiation, in the proposed antenna, the propagation and leakage of a quasi-TEM (Q-TEM) mode results in an extremely low-profile ($0.065\lambda_0$), high-gain ($\sim$15 dBi) antenna. In this scenario, the transverse resonance condition for a Q-TEM mode is established by employing a capacitive partially reflective surface (PRS) in a thin ($0.065\lambda_0$) substrate with a relative permittivity of 10.2. The proposed periodic 2DLWA, unlike the conventional uniform/quasi-uniform air-filled counterparts, radiates based on the n = −1 space harmonic operation. Due to a strong mutual interaction between the PRS and ground plane, conventional design and analysis approaches are no longer relevant in this low-profile architecture. Instead, we employ the Floquet modal expansion theory to create an equivalent circuit model (ECM) for the PRS that takes into account the contributions and mutual interactions of the Floquet harmonics as well as the ground plane effect. By employing reflecting boundaries realized with edge truncation (air trenches) in a high permittivity substrate, we show that the aperture efficiency is enhanced by 15% compared to conventional counterpart.

Index Terms—2-D leaky-wave antenna (2DLWA), EBG resonator antenna, Fabry–Perot cavity antenna (FPCA), Floquet modal expansion, high-gain antenna, low-profile antenna, optoelectronic integrated circuit (OEIC), partially reflective surface (PRS), PRS antenna, radio-over-fiber (RoF), resonant cavity antenna.

I. INTRODUCTION

THE seamless integration of an antenna with a frontend is of significant importance in the realization of high-efficient and low foot-print transceivers in millimeter-wave (mmW) and terahertz (THz) analog radio-over-fiber
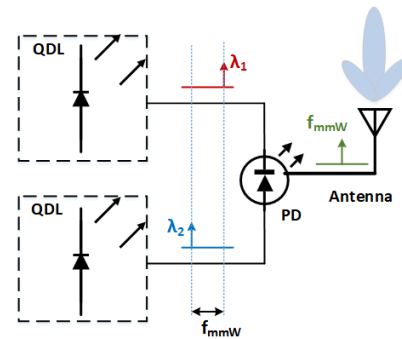
Fig. 1. General block diagram of an ARoF system.

(ARoF) systems. In upcoming ARoF systems, electrooptic modulator (EoM) and photodiode (PD) in an optoelectronic transceiver are basically implemented on a high permittivity material (e.g., SiGe, GaAs, and InP) with eventual heterogenous structured layers, which introduces fundamental hurdles in the design and integration of antennas with a frontend.

Fig. 1 shows a generalized block diagram for cutting-edge ARoF frontends [optoelectronic integrated circuits (OEICs)], in which electrical mmW/THz signal is generated by an efficient beating of two high-quality optical signals coming out of quantum dot lasers (QDLs) and mixed in a PD [1]–[3]. The use of a power amplifier generally introduces nonlinear behavior and loss into transceiver, inevitably increasing power consumption and complexity. Therefore, it is removed from the ARoF frontends, as shown in Fig. 1. Laser diodes, on the other hand, are set to operate at relatively low power; therefore, it is anticipated that adopting a high-gain and high-efficiency antenna becomes critical in this design to meet the desired link budget in an mmW/THz ARoF wireless link [3], [4].

A highly original integrated circuit (IC)-antenna approach studied and demonstrated in [5] can improve the performance and efficiency of an OEIC frontend by eliminating parasitic effects and extra losses caused by bond wires and matching networks. Furthermore, this technique requires less real estate in an on-chip transceiver. Therefore, as the next step toward creating an efficient frontend, achieving a low footprint, high-gain (high aperture efficiency), and low-profile antenna on a high permittivity substrate becomes crucial.

As a result, the work reported here is focused on developing a low-profile, compact, high-gain, and high-efficiency antenna

on a high permittivity substrate to fulfill the criteria of an OEIC-based frontend in an ARoF system.

A common approach to realizing a high-gain antenna is to create a massive planar antenna array. However, implementing such a massive antenna array at mmW and THz frequencies on a high permittivity substrate is deemed to create several significant problems, making it extremely difficult in practice. High confinement of electromagnetic (EM) fields in a substrate, which is set to reduce antenna efficiency and to generate slab or surface waves, tightly coupling of antennas through excited surface waves, excessive radiation loss in feeding lines, and so on, are some of the headache issues that severely degrade antenna performances.

Some strategies for achieving a high-gain and high-efficiency antenna array by suppressing surface waves and mutual couplings have been developed [6]–[8]. Although these approaches are still practical, they have the potential to increase system complexity and cost, as well as to make antenna integration cumbersome and complex.

Another intriguing option, namely, the 2-D leaky-wave antenna (2DLWA) (also known as the Fabry–Perot cavity antenna (FPCA), EBG resonator, and resonant cavity antennas), has been extensively explored in recent years [4], [9]–[62]. This high-gain antenna can generate a pencil beam using a simple structure, which makes it a promising alternative for the conventional planar antenna array in mmW and THz frequencies. Basically, its radiation mechanism is based on the propagation and leakage of the TE_1/TM_1 waves in a cavity realized by a ground plane and a capacitive/inductive partially reflective surface (PRS) [18]–[46] or multilayer superstrate [10], [12], [13], [16], [17], [62]. This cavity can be efficiently activated by a single slot [12]–[31] (in mmW and microwave) or multiple slots [35] etched on the ground plane (at 60 GHz) or a dipole antenna [32] (for X-band) aligned in the middle of the cavity, respectively, where magnetic and electric fields are maximum. Although this antenna exhibits some advantages over the other types of high-gain antennas, it typically suffers from two fundamental issues: 1) high-profile structure due to the use of TE_1/TM_1 modes that requires a large separation between the ground plane and PRS (cavity height) to satisfy the transverse resonance (TR) condition, which is a limiting factor in ICs design, and 2) typically low aperture efficiency that makes the antenna bulky and large.

Typically, the cavity height in a 2DLWA without the PRS loading effects is estimated as a half-wavelength $h = 0.5\lambda_0/\sqrt{\varepsilon_r}$ [27]. Considering the susceptance of the PRS, however, this height is evaluated as $h = (0.5\lambda_0/\sqrt{\varepsilon_r})(1 + \sqrt{\varepsilon_r}/\pi\bar{B})$ [27] (where $\bar{B}$ is the normalized susceptance of the PRS to the air admittance). As is evident for a capacitive PRS ($B > 0$), the required height will be larger than a half wavelength, while for an inductive PRS ($B < 0$) with a large susceptance (a high-gain antenna is realized by a large value of $\bar{B}$ [18], [27]), the cavity height approaches a half wavelength. Note that the typical and practical value of $\bar{B}$ is estimated with $\bar{B} = \pm\sqrt{((1 + \sqrt{\varepsilon_r})^2|\Gamma_{PRS}|^2 - (1 - \sqrt{\varepsilon_r})^2)/(1 - |\Gamma_{PRS}|^2)}$, where $|\Gamma_{PRS}|$ is the magnitude of the PRS reflection coefficient [32]. Basically, a high-gain antenna requires

$|\Gamma_{PRS}| > 0.9$, which results in $\bar{B} > +7$ [23], [32]. Therefore, the cavity height in a conventional 2DLWA using a substrate with $\varepsilon_r = 10.2$ with a capacitive PRS is evaluated as $h > 0.18\lambda_0$.

In this work, we show that by employing a low-profile capacitive PRS, whose susceptance is in a specific range (according to the developed equations and graphs in Section II), on a substrate of a large relative permittivity, a Q-TEM mode can be excited, which results in a very low-profile and high-gain 2DLWA. Full-wave simulations in Section III are set to validate the results obtained by the theory presented in Section II.

Generally, in this low-profile 2DLWA, the ground plane has a strong mutual interaction with a metallic PRS; therefore, conventional design and analysis methodology based on the evaluation of the reflection coefficient of a suspended PRS (in which the ground plane is removed in a unit cell and two ports are assigned at the top and bottom) cannot be applied. To address this issue, we developed a hybrid methodology based on the modal expansion of Floquet harmonics and full-wave analysis to evaluate the equivalent circuit model (ECM). In this methodology, the mutual coupling between the PRS and ground plane as well as mutual interactions between Floquet harmonics are considered. Full-wave simulations and analytical model of the radiation pattern in Section III verify the accuracy of the proposed ECM.

Looking at the literature, the aperture efficiency in these antennas was reported as 18%–32% [4] and 10%–20% [38] with an inductive PRS, up to 65% with a capacitive PRS [23], [32], and up to 86% by a multilayer transverse permittivity gradient PRS [62]. Although the latter type can provide a larger aperture efficiency, in this article, we focus on a low-profile metallic PRS, which can be used without air gap for OEIC application.

To address this issue, we show that the truncation of a PRS printed on a substrate with a large relative permittivity creates a reflecting boundary. An analytical model of the radiation pattern is employed, in which effects of boundaries' reflections are incorporated, to show the significant contributions of edge reflections to aperture efficiency. The analytical model is then validated by full-wave simulation results in Section III.

Total boundaries' reflections can be controlled by a proper choice of antenna dimensions (studied by parametric analysis). Parametric analysis shows that these reflecting boundaries can improve the aperture efficiency up to 15% compared to a conventional air-filled counterpart.

The rest of this article is organized as follows. In Section II, we discuss the fundamental theory of the capacitive PRS on a substrate with large relative permittivity. We also discuss the development of an ECM based on the EM full-wave simulator and Floquet modal expansion theory. In Section III, a 2DLWA is designed on Rogers RT/Duriod 6010 based on the developed theory presented in Section II, and then, dispersion diagrams are calculated. Having used the dispersion curves, we present a leaky-wave analysis for the antennas in this section. To select the proper design parameters, a parametric analysis is presented. In Section IV, an air-filled 2DLWA is designed, and its aperture
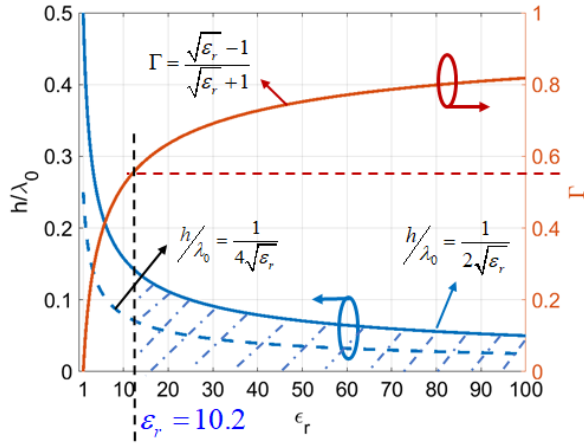
Fig. 2. Normalized height and reflection coefficient of lateral walls in a dielelctic-embedded PPW operating in the fundamental mode (TEM) with respect to the relative permittivity of substrate.

efficiency is compared with that of the proposed antenna. Finally, simulated and measured results are presented and discussed.

II. THEORY AND BACKGROUND

A. Capacitive PRS on a High Permittivity Substrate

A metallic parallel-plate waveguide (PPW) filled with a dielectric with large relative permittivity can be considered as a closed waveguide realized by perfect magnetic conductor (PMC)-like lateral walls in which the fundamental propagating mode (TEM mode) is a slow wave. As shown in Fig. 2, the reflection coefficient of the lateral walls for $\varepsilon_r \geq 10.2$ is larger than 0.5, implying that at least half of the power is reflected from the lateral boundaries. To satisfy the single-mode propagation conditions of the fundamental mode, high-order modes, including TE_1/TM_1 modes, should be in the cutoff frequency range. Therefore, the propagation constant of $\beta = \sqrt{\varepsilon_r k_0^2 - (\pi/h)^2}$ should be imaginary, which corresponds to $0 < \sqrt{\varepsilon_r} h/\lambda_0 < 0.5$ and the hatched region in Fig. 2. This area describes a region where only a TEM mode propagates in a closed PPW with PMC-like lateral walls. In this case, by introducing periodic perturbations in the top plate (i.e., PRS), a 2DLWA is realized in which the propagation and leakage of a quasi-TEM(Q-TEM) wave result in a high-gain antenna. The periodicity and types of perturbations determine the susceptance of the PRS.

To evaluate the susceptance of the PRS, a well-known transverse equivalent network (TEN) is employed, as shown in Fig. 3. In this case, a TR condition $imag(Y_{up} + Y_{down}) = 0$ [42] is satisfied when $B\eta = \cotan(\sqrt{\varepsilon_r} 2\pi h/\lambda_0)$, where B is the susceptance of the PRS, η is the wave impedance in the dielectric, h is the cavity height, and λ_0 is the free-space wavelength. For a capacitive PRS ($B > 0$), the argument of the cotan function should either be in the first or third quadrant. Considering the single-mode propagation condition in a PPW as $0 < \sqrt{\varepsilon_r} h/\lambda_0 < 0.5$ and practical realization of a 2DLWA with a capacitive PRS, a TR condition for Q-TEM mode could
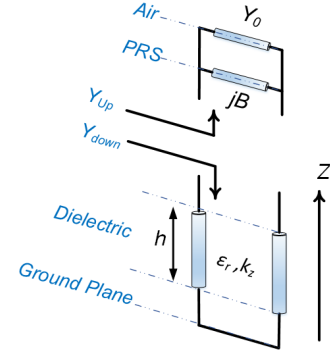

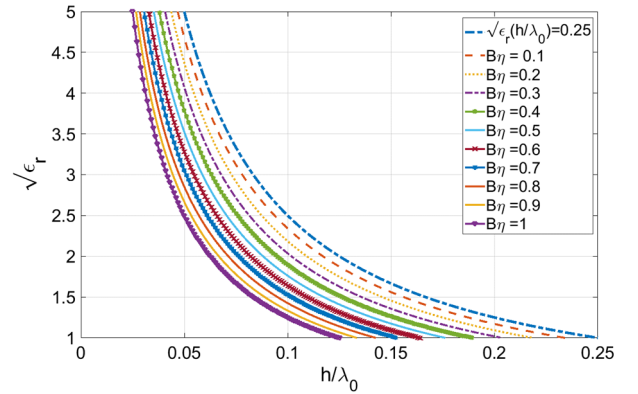Fig. 3. TEN model of a single-layer 2DLWA.

Fig. 4. Relative permittivity with respect to normalized height in a 2DLWA for different values of PRS susceptance.

be held when the capacitive PRS and PPW simultaneously satisfy (1) and (2). It should be noted that, in an inductive PRS with $B < 0$, the argument of a cotan function in the TR equation should be either in the second or fourth quadrant resulting in a higher profile 2DLWA compared to that of a capacitive PRS

$$0.1 < \sqrt{\varepsilon_r} \frac{h}{\lambda_0} < 0.25 \tag{1}$$

$$0 < B\eta < 1. \tag{2}$$

Having considered (1) and (2), we can develop a set of design curves for different values of $B\eta$, which can be employed for antenna design, as presented here in Fig. 4. As is well known in the 2DLWA theory, large values of normalized PRS susceptance ($\bar{B}$) result in a high-gain antenna [18], [27]. According to (2), one can readily find that $B\eta_0 = \bar{B} < \sqrt{\varepsilon_r}$; therefore, a dielectric-filled cavity with a large dielectric constant not only results in a low profile but also a high-gain antenna can be realized.

B. Equivalent Circuit Model of PRS

The standard design technique for a uniform/quasi-uniform PRS is based on evaluating the reflection coefficient of a suspended PRS in a unit cell with PEC and PMC boundary conditions [4], [18]. However, due to the use of high permittivity and also a relatively thin substrate in the proposed antenna,
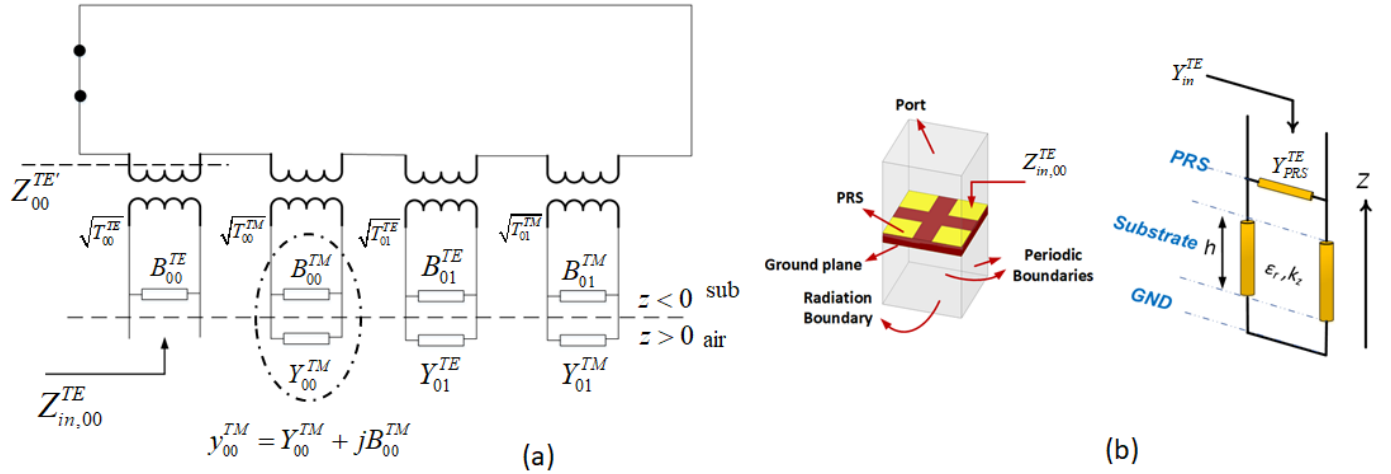
Fig. 5. (a) Equivalent circuit model of a PRS with Floquet modal expansion (b) with a corresponding typical unit cell and its equivalent transmission line (TL) model.

the ground plane should be included in the simulated model to incorporate the mutual interaction between the metallic PRS and the ground plane appropriately.

A typical analytical design technique based on the Bloch analysis, which ignores the mutual interaction between space harmonics, is thought to provide erroneous findings, particularly in the case of a high permittivity substrate and mmW regime. However, in this section, we intend to develop a hybrid design process based on full-wave simulation (HFSS) and the development of an ECM using the Floquet modal expansion theory.

Fig. 5(a) shows the proposed ECM developed for a typical unit cell, which includes a PRS over the grounded dielectric with periodic boundary conditions [Fig. 5(b)] [58], [59]. In this model, according to the Floquet modal expansion theory, $Z_{in,00}^{TE}$ is the input impedance of the unit cell for TE_{00} mode (fundamental Floquet harmonic for TE mode), which is evaluated with the HFSS at the air–PRS interface in the unit cell, as exemplified in Fig. 5(b) and described analytically in (3). It is worth mentioning that employing either TE_{00} or TM_{00} mode as incident waves in a normal direction leads to identical results

$$Z_{in,00}^{TE}(f) = \left(y_{in,00}^{TE}(f)\right)^{-1} = \left(T_{00}^{TE}\left(Z_{00}^{TE'}\right)^{-1} + jB_{00}^{TE}\right)^{-1}$$

$$Z_{00}^{TE'} = \sum_{m\neq0}\sum_{n\neq0} T_{mn}^{TE}\frac{1}{y_{mn}^{TE}} + \sum_{m=-\infty}^{+\infty}\sum_{n=-\infty}^{+\infty} T_{mn}^{TM}\frac{1}{y_{mn}^{TM}}$$

$$y_{mn}^{TM/TE} = Y_{mn}^{TM/TE} + jB_{mn}^{TM/TE}. \tag{3}$$

In (3), y_{mn}^{TE} and y_{mn}^{TM} are the modal admittance seen by TE_{mn} and TM_{mn} modes, respectively, at the air–dielectric boundary; T_{mn} is the transformer turn ratio (TTR); and jB_{00}^{TE} is the input modal admittance of the grounded dielectric slab (GDS). These parameters were entirely described in [58] and [59], and therefore, for the sake of brevity, we will not elaborate on them in this article. It should be noted that T_{00}^{TM} in Fig. 5(a) indicates mode conversion.

The only unknown parameters in (3) are T_{mn}^{TM} and T_{mn}^{TE} (TTRs). Analytical equations based on the Fourier

transformation of surface currents are developed in [58] and [59] to evaluate TTRs at low frequency and on a dielectric with low relative permittivity. Notably, the latter generally cannot be applied in a dielectric with large relative permittivity in mmW ranges. Therefore, we aim at calculating T_{mn}^{TM} and T_{mn}^{TE} over frequency band of interest through a full-wave simulation conducted by the HFSS.

By rearranging (3), one can readily find the following equation:

$$\underbrace{\left[\frac{1}{y_{in,00}^{TE} - jB_{00}^{TE}}\right]}_{K}$$
$$= \frac{1}{T_{00}^{TE}}\left(\sum_{m\neq0}\sum_{n\neq0} T_{mn}^{TE}\left(\frac{1}{y_{mn}^{TE}}\right) + \sum_{m=-\infty}^{+\infty}\sum_{n=-\infty}^{+\infty} T_{mn}^{TM}\left(\frac{1}{y_{mn}^{TM}}\right)\right) \tag{4}$$

$$\underbrace{\begin{bmatrix} [1/y_{mn}^{TE}]_{1\times N}^{f_1} & [1/y_{mn}^{TM}]_{1\times N}^{f_1} \\ \vdots & \vdots \\ [1/y_{mn}^{TE}]_{1\times N}^{f_N} & [1/y_{mn}^{TM}]_{1\times N}^{f_N} \end{bmatrix}}_{N\times(1\times 2N)} \underbrace{\begin{bmatrix} [T_{mn}^{TE}]_{N\times 1}^{f_1} \\ [T_{mn}^{TM}]_{N\times 1}^{f_1} \\ \vdots \\ [T_{mn}^{TE}]_{N\times 1}^{f_N} \\ [T_{mn}^{TM}]_{N\times 1}^{f_N} \end{bmatrix}}_{N\times(2N\times 1)}$$
$$= \underbrace{\begin{bmatrix} K^{f_1} \\ \vdots \\ \vdots \\ \vdots \\ K^{f_N} \end{bmatrix}}_{N\times(1\times 1)} \tag{5}$$

$$[T_{mn}^{TE/TM}] = [1/y_{mn}^{TE/TM}]^{-1}[K]. \tag{6}$$

The matrix representation of (4) is shown in (5), which is suitable for numerical programming. To evaluate the K matrix as mentioned in (5) and (4), we calculate $Z_{in,00}^{TE}$ and B_{00}^{TE} by HFSS and analytical equations mentioned in [58] and [59],
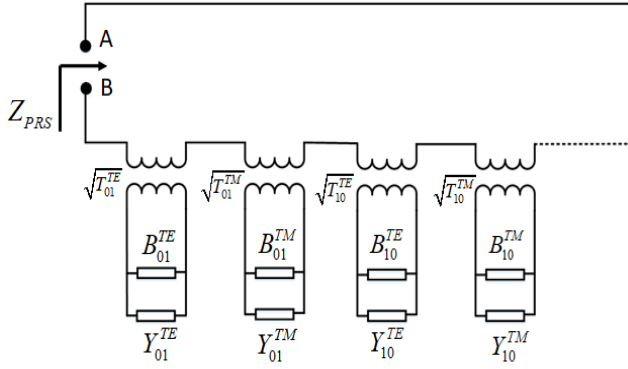
Fig. 6. ECM for evaluation of PRS susceptance.

Fig. 7. Proposed 2DLWA with dimensions of P = 4.8 mm ($w/p = 0.9$), P = 5.7 mm ($w/p = 0.75$), w = 4.3 mm, and L = 19.7 mm.

respectively, at each frequency point. Notably, for the benefit of simplicity in our calculations, we considered $T_{00}^{TE} = 1$ in this model.

Equation (5) can be considered as a 3-D matrix with N pages corresponding to N frequency points, where a total of $2N$ Floquet harmonics (corresponding to mn pairs) are applied for both TM and TE modes. Note that, considering only a few Floquet harmonics leads to an accurate result [56], [57]. Finally, the TTR matrix representing the contribution of each Floquet harmonic in the ECM is obtained using (6) in the desired frequency range.

Having evaluated the TTR matrix, one can readily calculate the circuit parameters of the PRS corresponding to the input impedance/admittance seen from the AB terminal in Fig. 6 and as described by (7). Note that the Floquet harmonics corresponding to TE_{00} and TM_{00} have been removed in this ECM since these radiative modes generate real-value impedances in the ECM, which do not contribute to the susceptance of the PRS. In Section III, we will apply this methodology for evaluating the ECM of a capacitive PRS

$$Z_{PRS} = \sum_{m \neq 0} \sum_{n \neq 0} \left(T_{mn}^{TE} [1/y_{mn}^{TE}] + T_{mn}^{TM} [1/y_{mn}^{TM}] \right)$$

$$= \left[T_{mn}^{TE} | T_{mn}^{TM} \right] \begin{bmatrix} 1/y_{mn}^{TE} \\ 1/y_{mn}^{TM} \end{bmatrix}_{mn \neq 0}$$

$$B_{PRS} = imag(1/Z_{PRS}). \tag{7}$$

III. ANTENNA DESIGN AND ANALYSIS

In this section, we aim at designing two 2DLWAs realized by a typical capacitive PRS in which a Q-TEM wave is responsible for generating high directive broadside beams. Following that, a leaky-wave analysis is presented to confirm the propagation of Q-TEM mode and findings in Section II. To investigate the effects of edge reflections on aperture efficiency, an analytical model is provided and validated using HFSS.

To begin with, we consider two different possible scenarios for PRS with $w/p = 0.75$ and $w/p = 0.9$, corresponding to periodicity $p = 5.7$ mm and $p = 4.8$ mm, respectively, on Rogers RT/duroid 6010 with $\varepsilon_r = 10.2$ and $\tan\delta = 0.0023$ at 26 GHz, as show in Fig. 7. Generally, periodicity is chosen
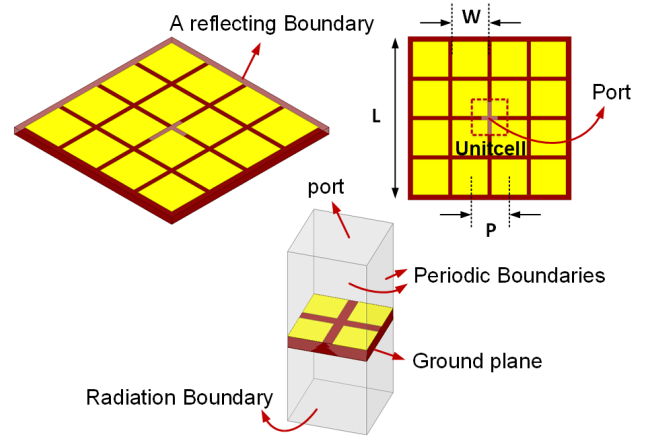
so that the antenna operates in a no grating lobe regime at the resonant frequency (a half free-space wavelength) [57].

Although this methodology can be extended to a broad range of capacitive PRS (e.g., dogbone [60]), we utilize square patches on a GDS as a proof of concept. A capacitive PRS is commonly achieved by a periodical repetition of metallic patches [27]. The PRS has been extended up to only a few unit cells (three unit cells in this design) to ensure that some nonradiated EM power remains at the truncated edges to be reflected, as this technique enhances the aperture efficiency of the 2DLWA. This is scrutinized by analytical equation and parametric analysis in this section.

Now, we use the analytical set of equations developed in Section II-A as the starting point for design, and then, a full-wave analysis by HFSS is employed to optimize and validate the results.

According to (1), the normalized cavity height for exciting a Q-TEM mode in a 2DLWA with a capacitive PRS on a dielectric with $\varepsilon_r = 10.2$ is evaluated as $h/\lambda_0 < 0.078$. This limit can be found readily in Fig. 2 at the intersection point of two labeled broken lines corresponding to $\varepsilon_r = 10.2$ and $h/\lambda_0 < 0.25/\sqrt{\varepsilon_r}$.

Considering this range along with $\varepsilon_r = 10.2$ in Fig. 4, the optimal normalized susceptance for the PRS is found to be $0.3 < B\eta < 1$ (η is the wave impedance in dielectric) corresponding to 2.54 mS $< B < 8.47$ mS. Starting with a substrate thickness within the range of $h/\lambda_0 < 0.078$ as the initial value, we optimize the substrate thickness for both antennas with $w/p = 0.9$ and $w/p = 0.75$ using HFSS at 26 GHz to obtain the maximum directivity at the broadside, as shown in Fig. 8. It is worthwhile stressing that, the maximum normalized substrate thickness is limited to around $h/\lambda_0 \approx 0.078$ preventing the antenna from propagating high-order modes, which should be considered in the optimization procedure. The calculated optimum thickness is evaluated around $h = 0.754$ mm corresponding to $h/\lambda_0 = 0.065$ at 26 GHz for both antennas. Evaluated broadside directivities of the antennas are 15.74 and 12.17 dBi corresponding to $w/p = 0.9$ and
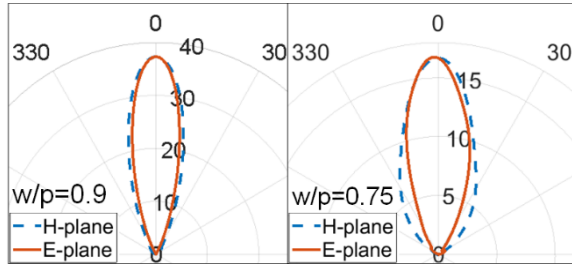
Fig. 8. Simulated directivities (with linear scales) of the proposed antennas corresponding to $w/p = 0.9$ and $w/p = 0.75$.
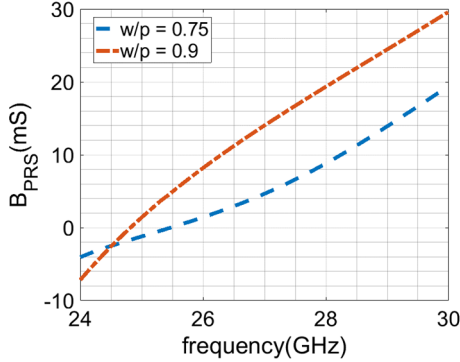

Fig. 9. Evaluated PRS susceptance of the proposed antenna by ECM for two values of $w/p = 0.9$ and $w/p = 0.75$ ($Y_{PRS} = jB_{PRS}$).
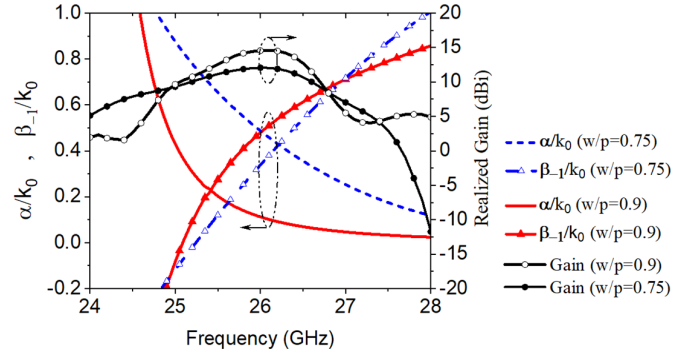

Fig. 10. Evaluated dispersion curves by (8) along with realized gain calculated by HFSS for both values of $w/p = 0.9$ and $w/p = 0.75$.

$w/p = 0.75$, respectively. Further analyses and validations of propagating mode are accomplished by a leaky-wave analysis presented in Section III-A.

A. Leaky-Wave Analysis of Antenna

Leaky-wave analysis is presented in this section to evaluate the obtained results and validate the proposed theory. Moreover, this analysis offers a physical insight into the antenna operation. To this end, the susceptance of PRSs was evaluated by the proposed ECM for both $w/p = 0.75$ and $w/p = 0.9$ and the results are presented in Fig. 9. In the model, we consider a total number of 30 Floquet harmonics for both TM and TE modes.

According to the proposed analytical evaluations in Section II along with current section, the optimum susceptance of PRS at 26 GHz should be in the range of 2.54 mS $< B <$ 8.47 mS. As shown in Fig. 9, the susceptance of the PRS with $w/p = 0.9$ is $B \approx 8.1$ mS, which is in the optimum range, while this is not the case for $w/p = 0.75$ with $B \approx 1.5$ mS. Therefore, one can infer that $w/p = 0.9$ results in an optimum design satisfying the TR condition. This antenna ($w/p = 0.9$) also presents a higher directivity by a full-wave simulation (HFSS) compared to that of $w/p = 0.75$, as shown in Fig. 8.

To evaluate the phase and attenuation constant, the TR technique is applied to the TEN model shown in Fig. 3, for both antennas according to the following equation:

$$Y_0 + jB - j\sqrt{\varepsilon_r}Y_0 \cot an \, (k_z h) = 0 \qquad (8)$$

where Y_0 is the air admittance, B is the susceptance of PRS, h is the cavity height, $k_z = \sqrt{\varepsilon_r k_0^2 - (\beta - j\alpha)^2}$ is the propagation constant in the normal direction (z-axis in Fig. 3), and k_0 is the free-space wavenumber. Dispersion curves (for $n = -1$ space harmonic) along with realized gains (evaluated by HFSS) for both antennas are shown in Fig. 10. At 26 GHz, the antenna with $w/p = 0.9$ shows a smaller attenuation constant and a larger realized gain (14.9 dBi) by 2.9 dBi compared to the antenna with $w/p = 0.75$ with a realized gain of 12 dBi. Therefore, we select an antenna with $w/p = 0.9$ in the rest of this article as the optimum design. Note that in Fig. 10, peak gain for $w/p = 0.9$ occurs at the frequency corresponding to $\beta > \alpha$, which is due to edge reflections [32], [50]–[52], while in $w/p = 0.75$, peak gain is very close to the $\beta = \alpha$ condition, as this antenna has a larger attenuation constant consequently; edge reflections are diminished.

To provide a further investigation about the propagation and radiation of a Q-TEM in the cavity, Fig. 11 compares the evaluated dispersion curves of the antennas with those of the fundamental mode of a PPW (TEM mode) and TM_0 mode of surface waves in a GDS for both $n = -1$ and $n = 0$ of space harmonics. Notably, in the fast wave region (FWR), the antennas' dispersion diagrams can be estimated as a weak perturbation of the TEM mode of a PPW around 26 GHz (corresponding space harmonics are quite similar around 26 GHz). As perturbations (corresponding to the attenuation constants shown in Fig. 10) are diminished with frequency, the dispersion curves of antennas approach more TEM mode curves. Consequently, in both antennas, radiations are due to the $n = -1$ space harmonics of a Q-TEM, as these space harmonics are in the FWR around 26 GHz. Surface waves, however, do not contribute to the radiations as their dispersion curves are quite divergent from those of the antenna in the FWR around 26 GHz.

To validate the ECM, Fig. 12 compares the input susceptance of the unit cell obtained by a full-wave simulation [$B_{in}^{TE} = imag(1/Z_{in}^{TE})$ in the unit cell in Fig. 5(b)], with that calculated in (9) according to its equivalent TL model [c.f. Fig. 5(b)]

$$B_{in}^{TE} = imag\left(Y_{PRS}^{TE} - jY^{TE} \cot an \, (k_z h)\right) \qquad (9)$$
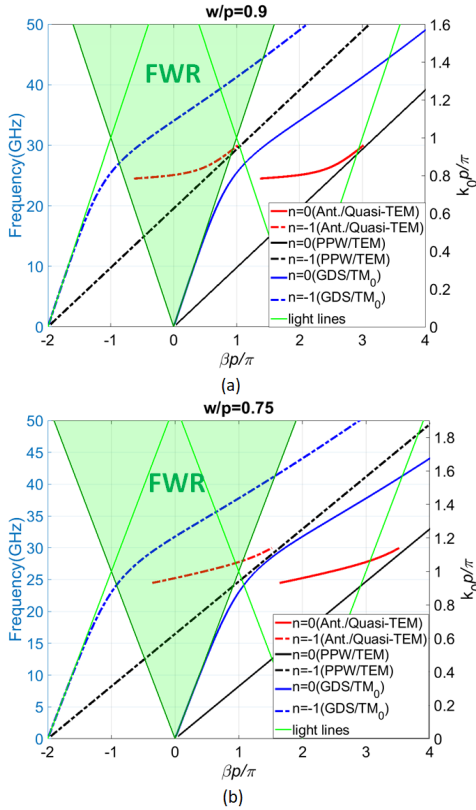
Fig. 11. Evaluated dispersion curves (Brillouin diagram) of fundamental modes ($n = 0$) and $n = -1$ space harmonics of the proposed antennas for two values of (a) $w/p = 0.9$ and (b) $w/p = 0.75$, along with dispersion curves of fundamental modes ($n = 0$) and $n = -1$ space harmonics of both TEM mode of a PPW and TM_0 mode of the surface wave in a GDS.

where $Y_{PRS}^{TE} = jB_{PRS}^{TE}$ is PRS admittance evaluated by ECM in Fig. 9, $Y^{TE} = k_z/\omega\mu_0$, $k_z = \sqrt{\varepsilon_r k_0^2 - (\beta - j\alpha)^2}$ in which β and α are transverse phase and attenuation constants, respectively, according to Fig.10, and h is the substrate thickness. Note that, radiation, ohmic, and substrate losses in a unit cell are negligible; therefore, the input admittance (Y_{in}^{TE}) of a unit cell is primarily dictated by its susceptance part (B_{in}^{TE}). A good agreement between HFSS and TL model results verifies the accuracy of the evaluated ECM and transverse propagation constant.

B. Analytical Model for Antenna

The far-field radiation pattern of an infinitely extended 2DLWA was accurately modeled by either the Fourier transformation of aperture field or reciprocity term along with TL model [18], [27], [49]. An analytical equation was developed in [32], [50], and [51] for a finite but large 2DLWA in which the effects of truncated edges were considered in a far-field radiation pattern. In [52], edge reflections are also considered in a 1-D uniform leaky-wave antenna (LWA) with a small linear aperture to describe the far-field radiation pattern, which forms the basis of our model in this work.

In the proposed periodic 2DLWA, radiation occurs at discrete points corresponding to the air gap between patches. Therefore, a discrete form of the equation is employed to
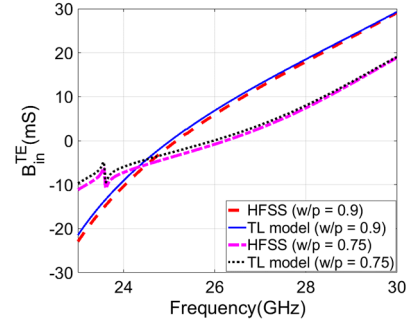

Fig. 12. Comparison between input susceptance of the unit cell in Fig. 5(b) obtained by a full-wave simulation (HFSS) and TL model for both $w/p = 0.75$ and $w/p = 0.9$.
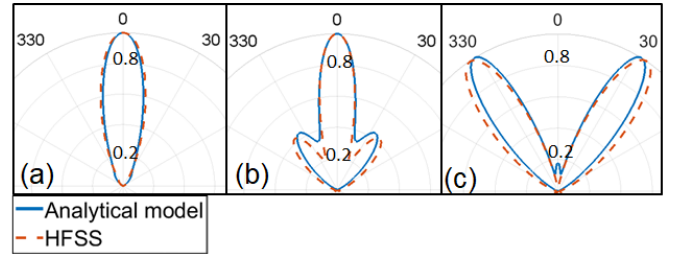

Fig. 13. Comparison between normalized radiation patterns evaluated by the analytical model and HFSS for the proposed 2DLWA with $w/p = 0.9$ at three simulation frequencies of (a) 26 GHz (model: 25.9 GHz), (b) 26.5 GHz (model: 26.35 GHz), and (c) 27 GHz (model: 26.9 GHz).

describe aperture field distribution (f_{ap}) and far-field radiation (corresponding to the discrete form of the Fourier transformation) of the antenna according to (10) and (11), respectively. In these equations, np denotes the unit-cell position in which "p" is periodicity and n is a variable; N is the total number of complete unit cells; $\Gamma \approx (\sqrt{\varepsilon_r} - 1)/(\sqrt{\varepsilon_r} + 1)$ is the reflection coefficient of a TEM/Q-TEM wave at the boundaries; $k_{LW} = \beta - j\alpha$; k_0 is the free-space wavenumber; and $L = N \times p$ represents the total antenna length.

Fig. 13 compares the normalized patterns calculated by (11) and HFSS at three different frequencies. A good agreement (frequency deviation $< 1\%$) is observed between the analytical model and the full-wave simulation signifying dominant contributions of the leaky-waves in far-field radiation, although the slot etched on the ground plane may have some minor contributions in the radiation pattern. Moreover, it implicitly verifies the accuracy of the evaluated ECM and dispersion curves

$$f_{ap}(np) = e^{-jk_{LW}|np|}$$
$$+ 2\cos(k_{LW}(np))\left(\Gamma e^{-jk_{LW}L}/\left(1 - \Gamma e^{-jk_{LW}L}\right)\right)$$
(10)

$$F^{ff}(\theta) = \cos\theta \sum_{n=-(N-1)/2}^{(N-1)/2} f_{ap}(np)e^{jk_0(np)\sin\theta}.$$
(11)

The second term in (10) indicates the contribution of the edge reflection coefficient in broadside directivity and aperture efficiency according to $\varepsilon_{ap} = D/4\pi(L/\lambda_0)^2$, where D is the antenna directivity at broadside, L is the antenna length, and λ_0
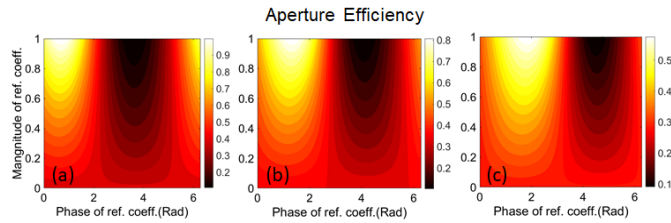
Fig. 14. Contour map of aperture efficiency with different values of edge reflection coefficient for three typical normalized leaky-wave poles of $k_{LW}^{-} = \bar{\beta} - j\bar{\alpha} = $ (a)$0.1 - j0.2$, (b)$0.2 - j0.2$, and(c) $0.3 - j0.2$.

is the free-space wavelength. Aperture efficiency is evaluated using (10) and (11) with $L = 20$ mm and p $= 4.8$ mm and three typical normalized leaky-wave propagation constants of $k_{LW}^{-} = \bar{\beta} - j\bar{\alpha} = 0.1 - j0.2, 0.2 - j0.2$, and $0.3 - j0.2$ with respect to the magnitude and phase of the edge reflection coefficient, as shown in Fig. 14. Obviously, the aperture efficiency is a function of the edge's reflections and can be improved by choosing a proper boundary condition. As an example, for $k_{LW}^{-} = 0.1 - j0.2$, if $\Gamma = 0$ (no edge reflections or absorbing boundaries), the aperture efficiency is around 30%–40% and can be improved up to 90% by employing a reflecting boundary with $\Gamma \approx j$. Therefore, in a 2DLWA by choosing the proper antenna length (which can control the edge contribution), the aperture efficiency can be enhanced, as investigated in Section III-C.

C. Parametric Analysis of the Proposed 2DLWA

Fig. 15(a) shows the antenna performances with respect to different lengths normalized to the free-space wavelength at 26 GHz. Note that in this analysis, the substrate height is fixed at 0.754 mm, as calculated in Section III. We define a figure of merit (FoM) as the ratio of broadside directivity over peak directivity to describe beam-splitting conditions. According to this definition, the FoM equal to one corresponds to peak directivity at the broadside and antenna presents a single broadside beam. In the case of a gain loss at the broadside, the FoM is smaller than one. A complete beam-splitting condition, manifested as a large gain loss at broadside, is defined as FoM < 0.5 in which directivity (realized by a power pattern calculated by HFSS) at the broadside is diminished by 3 dBi.

As shown in Fig. 15(a), the aperture efficiency has two peaks around $L/\lambda_0 = 0.8$ and $L/\lambda_0 = 1.7$ without gain loss at the broadside as indicated by $FoM = 1$. Then, at $L/\lambda_0 > 2.4$, the antenna experiences a beam-splitting condition. Since the aperture size at $L/\lambda_0 = 0.8$ is much smaller than that at $L/\lambda_0 = 1.7$, likewise, the corresponding directivity and realized gain are much lesser than those of at $L/\lambda_0 = 1.7$. In the case of $L/\lambda_0 = 0.8$, due to a small aperture size, radiation from the slot in the ground plane dominates the leaky-wave radiation as the antenna has a substantially lower realized gain than $L/\lambda_0 = 1.7$. The optimum length for the antenna is then selected at $L/\lambda_0 = 1.7$ corresponding to three complete unit cells at 26 GHz. At this length, the aperture efficiency of the antenna is 79%.
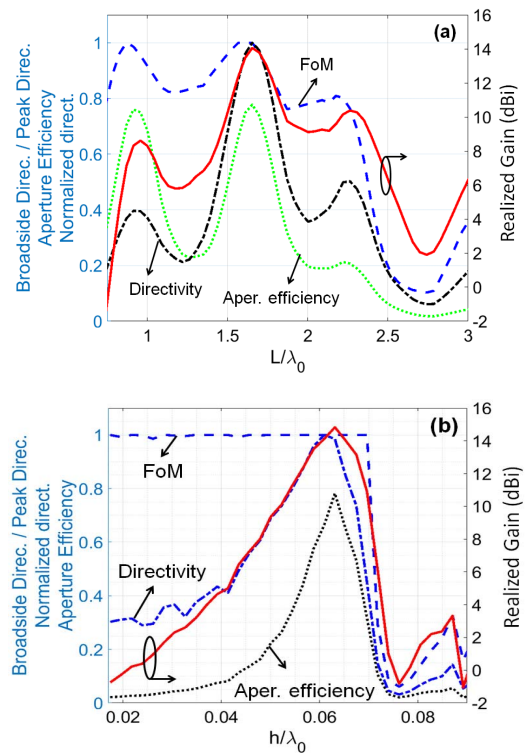

Fig. 15. Parametric analysis of the proposed 2DLWA for various values of (a) normalized cavity length and (b) normalized cavity height at 26 GHz.

Further investigation reveals that the field is attenuated at the edges by a factor of $E(L/2)/E_0 \approx \exp(-\alpha L/2)$, where E_0 is the field intensity at the antenna's center and "L'' equals an antenna length in a uniform/Q-uniform LWA [18]. Since the proposed periodic 2DLWA radiation occurs at discrete points, in this equation, $L = N \times p$, where N is a total number of complete unit cells, p $= 4.8$ mm is periodicity, and $\alpha = 60.1$ Np/m (Fig. 10 at 26 GHz for $w/p = 0.9$) is the attenuation constant. In this antenna at the operating frequency, the field ratio is 0.65, which corresponds to a 0.42 power ratio. This signifies edge contributions in antenna since 42% of the power at antenna's center reaches the edge.

The parametric study of the antenna height (with a fixed substrate length of $L/\lambda_0 = 1.7$) at 26 GHz, in Fig. 15(b), indicates that the optimum cavity height is around $h \approx 0.065\lambda_0$, which suggests a very low-profile antenna and verifies findings in Section III. As discussed in Section I, a typical cavity height in a conventional substrate-filled 2DLWA [operates based on the first higher order mode (TE$_1$/TM$_1$)] with $\varepsilon_r = 10.2$ is around $h = 0.18\lambda_0$. This offers a high-profile antenna with a substrate around three times thicker than in the proposed 2DLWA.

As the FoM indicates, the antenna has a splitted beam for $h/\lambda_0 \geq 0.072$. It can be attributed to the propagation of high-order modes according to Section III, in which the propagation of the high-order mode is estimated at $h/\lambda_0 \geq 0.078$.

IV. CONVENTIONAL AIR-FILLED 2DLWA

For the sake of a fair comparison, we developed and analyzed a conventional air-filled uniform 2DLWA based on
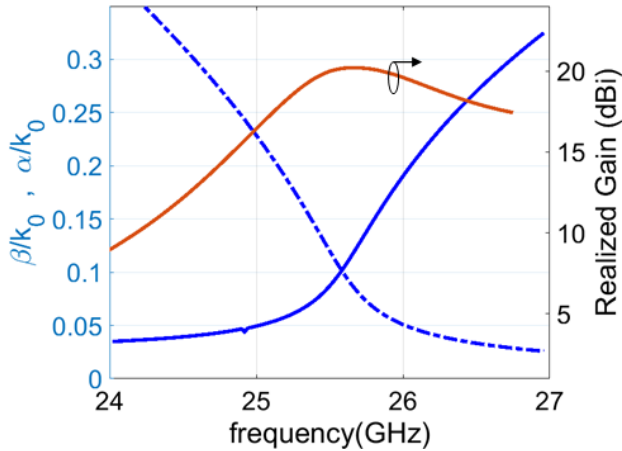
Fig. 16. Evaluated dispersion curve for the developed air-filled 2DLWA along with realized gain calculated by HFSS.

the design procedure mentioned in [4] and [32]. A capacitive PRS printed on a 20 mil Rogers RT/duroid 5880 dielectric is separated from the ground plane with a 5.8 mm air gap. The antenna operates based on the propagation of the first higher mode of a PPW. An opening etched on the ground plane efficiently excites the TE_1/TM_1 modes in the cavity [27]. Antenna parameters have been calculated and optimized to achieve the maximum realized gain at the broadside. The dispersion diagram is evaluated by the TR technique [32] and shown in Fig. 16 along with realized gain obtained by a full-wave simulation.

A. Parametric Analysis of Air-Filled 2DLWA

The antenna performance has been scrutinized with parametric analysis of the length and height, as shown in Fig. 17. A beam-splitting condition (based on the defined FoM) occurs at $L/\lambda_0 = 5.8$, as shown in Fig. 17(a). The estimated beam-splitting condition is consistent with analytical results in [32] as indicated here with a triangular curve. The aperture efficiency generally has a declining trend and reaches 64% at maximum antenna gain around $L/\lambda_0 = 3.4$, which is consistent with the 65% aperture efficiency mentioned in [23] and [32].

Parametric analysis for the antenna height in Fig. 17(b) clearly shows that the resonance condition occurs at $h/\lambda_0 = 0.5$ as is the case for the conventional air-filled 2DLWA. The defined FoM indicates that below $h/\lambda_0 = 0.44$, the antenna experiences a beam-splitting condition (a conical beam [18], [27]). The presented parametric analyses reveal that the aperture efficiency in the proposed 2DLWA on a high permittivity substrate is enhanced by 15% compared to conventional air-filled counterpart. This attributes to employing edge reflections in the proposed antenna, which can be readily realized by etching air slots around the PRS printed on a high permittivity substrate.

V. SIMULATION AND MEASUREMENT RESULTS

Antennas have been completely designed with optimum dimensions and feeding lines based on the parametric analysis,
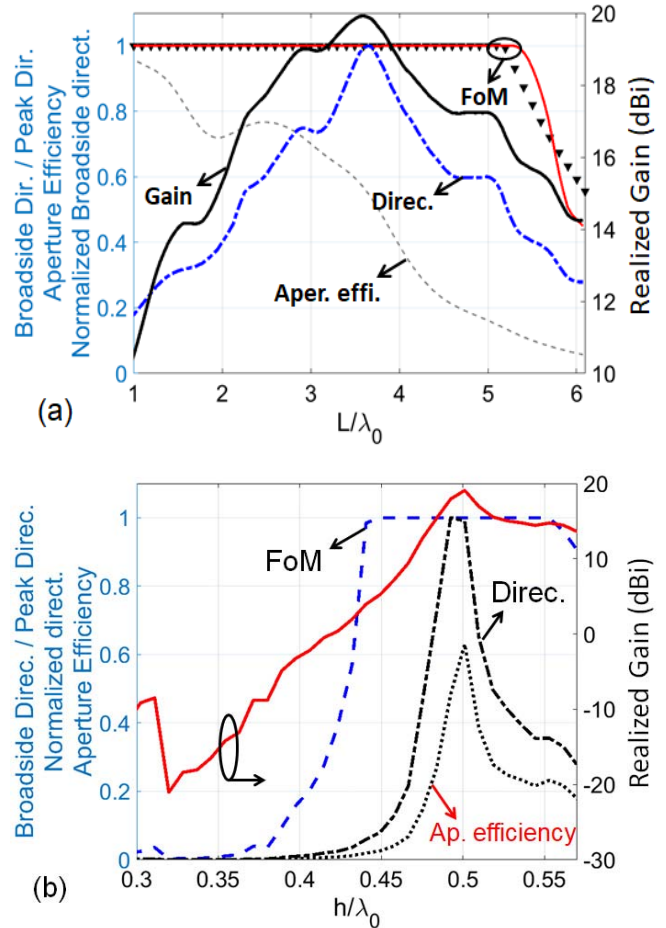

Fig. 17. Parametric analysis of the developed air-filled 2DLWA for various values of (a) normalized length and (b) normalized height at 26 GHz.

as shown in detail in Fig. 18. To eliminate the spurious effects of the feeding line on radiation behavior and excitation of surface waves, we take advantage of the SIW to realize a completely isolated antenna from the feeding network. The SIWs are implemented on Rogers RT/duroid 5880 with a thickness of 20 mil for both antennas to reduce loss and achieve mechanical stability for the fabrication process and measurement. A narrow aperture is etched at the end of the shorted SIWs (where the magnetic field is maximum) to ensure that cavities are excited efficiently.

We use a low-cost standard printed circuit board (PCB) process in our Poly-Grames Research Center for the fabrication of the antennas. Fig. 19(a) shows the fabricated proposed 2DLWA on Rogers RT/duroid 6010 with a relative permittivity of 10.2 along with the SIW feeding line. According to the parametric analysis of the proposed antenna, a substrate with a thickness of 0.754 mm results in a peak gain of 15 dBi. However, this thickness is not in the range of commercial substrates provided by Rogers Corporation.

Instead, we use a stack of three 10 mil layers that were tightly pressed and glued using epoxy to synthesize a unified substrate with the desired thickness and uniform connections between layers. In this antenna, substrates are extended enough
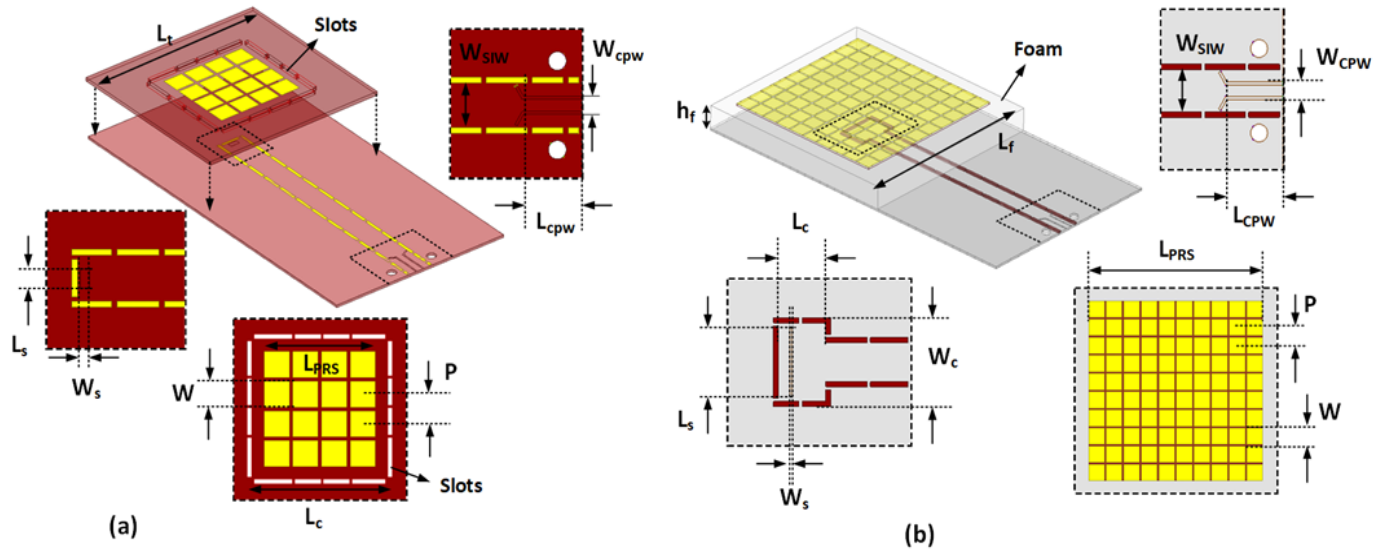
Fig. 18. Geometric and dimensions of (a) proposed 2DLWA with $L_{PRS} = 18.6$, $W_{SIW} = 4.8$, $W_{CPW} = 1.9$, $L_{CPW} = 6.5$, $L_t = 40$, $L_c = 20$, $W = 4.3$, $P = 4.8$, $W_s = 1$, and $L_s = 2$, and (b) air-filled FPCA with $L_{PRS} = 41.5$, $W_{SIW} = 4.8$, $W_{CPW} = 1.9$, $L_{CPW} = 6.5$, $L_f = 50$, $h_f = 5.8$, $W_s = 0.25$, $L_s = 8.5$, $W_c = 10.8$, $L_c = 7.2$, $P = 4.2$, and $W = 3.8$ (all dimensions are in millimeter).
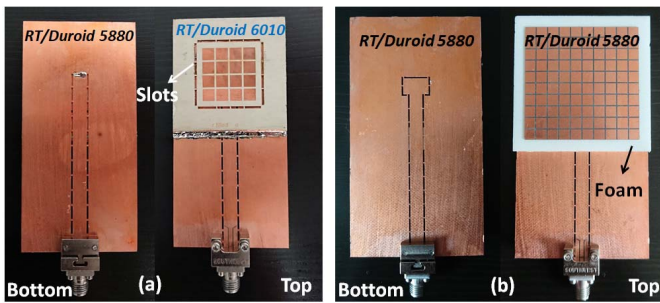

Fig. 19. Top and bottom views of (a) proposed and (b) air-filled 2DLWA.

Fig. 20. Simulated and measured reflection coefficients of the proposed 2DLWA. [L_s is the length of aperture etched on the ground plane according to Fig. 18(a).]

beyond the optimum size of the PRS to ensure that a negligible amount of epoxy glue leaks into the cavity. This extended area is separated by air trench/slot walls from the cavity to realize reflecting boundaries. Fig. 19(b) shows a snapshot of the fabricated conventional air-filled 2DLWA. The capacitive PRS is printed on Rogers RT/duroid 5880 with a thickness of 20 mil and separated from the SIW by a 5.8 mm air gap ($\sim \lambda_0/2$), realized with a ROHACELL foam. The PRS layer, foam, and the SIW layer were glued and then pressed. The high-density (71 kg/m^3) foam was deployed to provide sufficient mechanical strength during the fabrication process as well as reduce fabrication tolerances.

To mitigate loss and parasitic effects introduced by the foam inside the cavity, a large air hole is etched inside the foam. Then, the foam was extended beyond the PRS to reduce leakage of the epoxy glue inside the cavity.

A. Simulated and Measured Results of the Proposed 2DLWA

The reflection coefficients of both antennas were measured by the Keysight network analyzer (PNA N5247B). Fig. 20 compares the measured and simulated reflection coefficients of the 2DLWA on a high permittivity substrate.
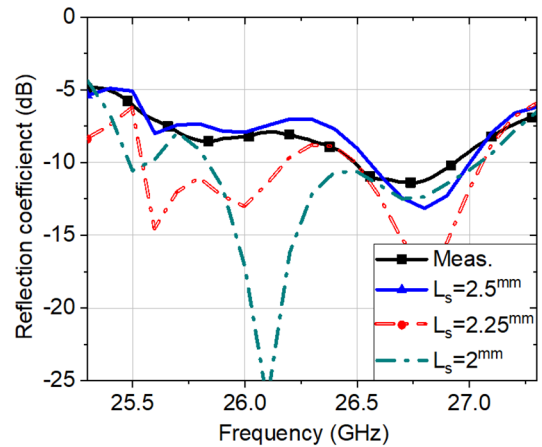
Some discrepancies are observed between simulation and measurement results that are due to fabrication tolerances and can be explained by sweeping the slot length [L_s in Fig. 18(a)] etched at the end of the shorted SIW. The simulated fractional impedance bandwidth ($VSWR \leq 2$) corresponding to $L_s = 2$ mm is around 5.3% while, due to 0.5 mm inaccuracy in slot length in the fabricated prototype, the measured fractional impedance bandwidth for $L_s = 2.5$ mm is about 2.2%. It denotes the sensitivity of impedance matching to the slot length, which should be carefully considered in antenna-frontend integration.

The simulated radiation and aperture efficiencies of the 2DLWA at 26 GHz are 96% and 79% (up to 80% around 26.1 GHz), respectively, as shown in Fig. 21.

Note that the antenna experiences a slight frequency shift compared to the parametric analysis, which is due to
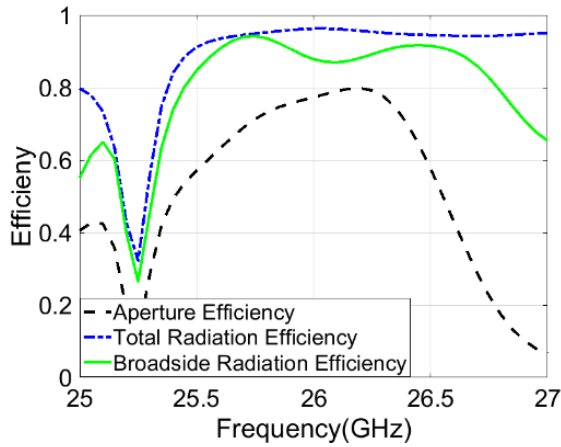
Fig. 21. Simulated total, aperture, and broadside efficiencies of the proposed 2DLWA.
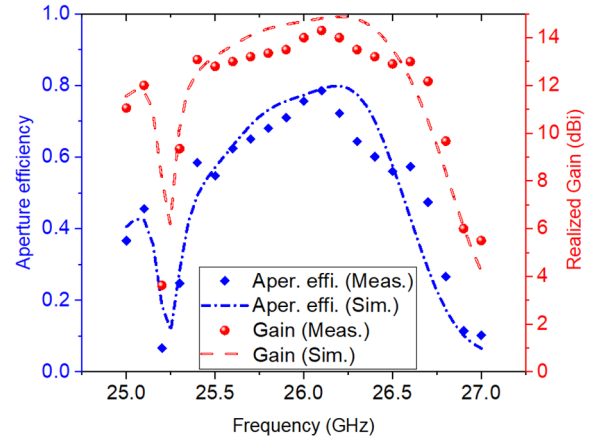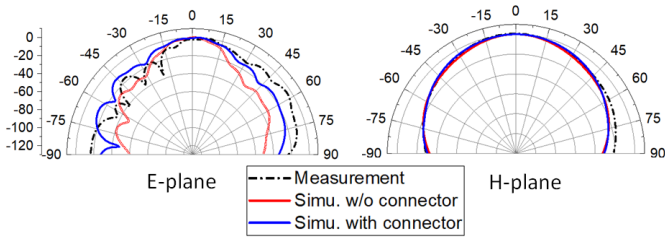

Fig. 22. Normalized simulated and measured copolarization radiation pattern of the proposed 2DLWA with and without connector effects including adhesive with 2 mil thickness.
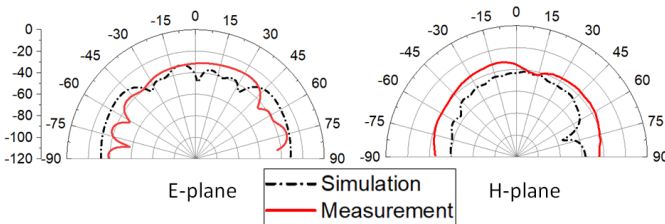

Fig. 23. Simulated and measured cross-polarization radiation patterns of the proposed 2DLWA with connector effects including adhesive with 2 mil thickness.
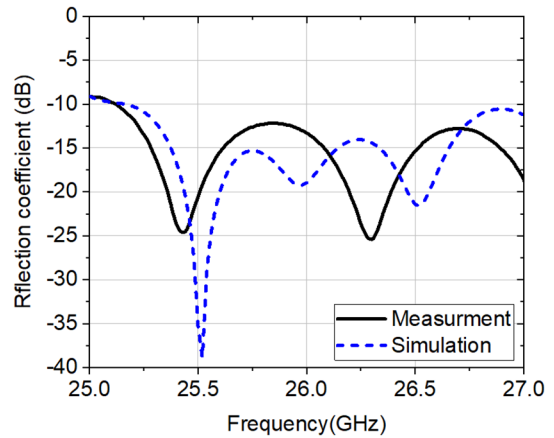

Fig. 24. Simulated results and experimental validations of realized gain and aperture efficiency of the proposed 2DLWA.

Fig. 25. Simulated and measured reflection coefficients of the air-filled 2DLWA.

both datasets in the E-plane of co-polarization pattern, which can be attributed to diffractions from the end-launch connector during measurement, as shown in Fig. 22.

Measured and simulated broadside realized gains along with aperture efficiency in the frequency range of 25–27 GHz are plotted in Fig. 24. A reasonable agreement is observed between simulation and experimental results. The minor discrepancies (<1 dBi) in realized gain around the operating frequency (26 GHz) are mostly due to fabrication tolerance in slot length (L_s), as estimated in Fig. 20. The measured and simulated peak realized gains are around 14.45 and 15 dBi, respectively. As shown in Fig. 24, the measured aperture efficiency properly follows the simulated result with a reasonable agreement.

B. Simulated and Measured Results of Air-Filled 2DLWA

As shown in Fig. 25, the measured reflection coefficient is in proper agreement with simulated results in air-filled 2DLWA. Fig. 26 shows the simulated and measured radiation patterns in both E- and H-planes of this antenna at 26 GHz. As studied by parametric analysis in Fig. 26, some disagreements between experimental and simulation results are due to minor

introducing the feeding line. Broadside radiation efficiency is also plotted in Fig. 21, which is defined as the ratio of broadside gain over broadside directivity [4]. As plotted, the broadside radiation efficiency in the proposed antenna is about 89% at 26 GHz.

The antenna's radiation patterns were measured in our Poly-Grames Research Center's far-field anechoic chamber, and the results are detailed in the following. The antenna under test (AUT) in the measurement setup receives a radiated EM power from a transmitter, which is an mmW horn antenna. To evaluate the gain of the AUT, a standard gain horn (SGH) antenna (NSI-MI Technologies Model: MI-12A-26) was employed.

Figs. 22 and 23 compare the simulated and measured co-polarization and cross-polarization radiation patterns of the proposed antenna. Some discrepancies are observed between

TABLE I
COMPARISON OF THE PROPOSED AND REFERENCE ANTENNAS

Ref.	Antenna profile $(\lambda_0)^1$	Peak Aperture efficiency (%)	Peak gain (dBi)	Impedance BW (%)	Gain BW (%)[2]	Cavity Footprint $(\lambda_0^2)^1$	Cavity type	Frequency (GHz)[3]
[5]	0.5	18~35	15.6	7.8	4.29	21.34 (4.62×4.62)		63
[17]	0.81	51	16.6	16.7	-	6 (3×2)		9.9
[23]	0.5	65	20.07	4.7	-	18.1 (4.25×4.25)		8.5
[24]	0.254	26.2	16	11.5	3.6	12.11 (3.48×3.48)	Rectangular, air filled	60
[32]	0.51	65	20	-	2.88	13.47 (3.67×3.67)		10.5
[38]	> 0.4	10~20	13.6	-	25.6	10.0 (3.17×3.17)		61.4
[43]	0.2	19.21	12.77	58.1	34.8 & 46	7.84 (2.8×2.8)		8.5
[61]	0.96	27.82	21	13.4	2.92	36 (6×6)		12
[62]	1.29	86	20.2	47.2	57	11.15	Circular, air filled	14.5
This work	0.065	Meas.: ~78.7 Sim.: 80	Meas.: ~14.45 Sim.: 15	Meas.: ~ 2.2 Sim.: 5.3	Meas.: 4.83 Sim.: 4.9	2.9 (1.71×1.71)	Rectangular, dielectric filled (ε_r = 10.2)	26.1

[1]: λ_0 is calculated at the antenna's peak performance.
[2]: 3dBi variations is considered in bandwidth calculation.
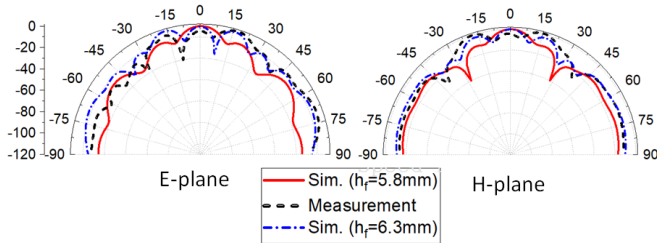[3]: Frequency of antenna's peak performance.

Fig. 26. Normalized simulated and measured radiation patterns of the air-filled 2DLWA at 26 GHz. [h_f is the cavity height as shown in Fig. 18(b).]
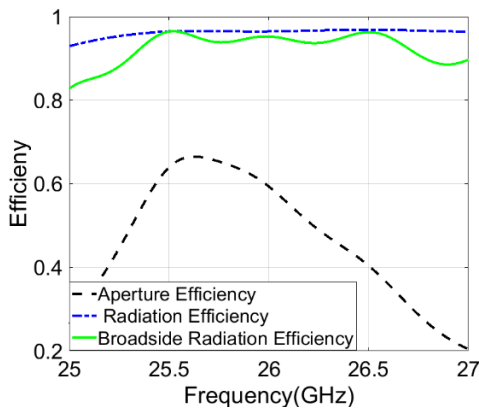

Fig. 27. Simulated aperture, total, and broadside efficiencies in the air-filled 2DLWA.

deviations in cavity height realized by foam as justified for both principal planes.

The simulated aperture efficiency in Fig. 27 is around 60% at 26 GHz, while it has a peak of 65% around 25.68 GHz. Total radiation efficiency and broadside radiation efficiency are 96% and 93%, respectively.

It is worth mentioning that the simulated broadside realized gain in this antenna is 20 dBi.

C. Comparison Table

To highlight the advantages of the proposed 2DLWA, a comparison table is provided, as tabulated in Table I. It demonstrates that the proposed antenna outperforms other published counterparts judging from the combination of antenna profile, aperture efficiency, and cavity footprint, for OEIC applications. Although the proposed antenna provides a lower impedance and pattern bandwidth than certain air-filled counterparts due to the use of a substrate with a high relative permittivity (ε_r = 10.2), it is still a viable candidate for antenna-front integration.

VI. CONCLUSION

An extremely low-profile, low-footprint, and highly efficient mmW 2DLWA on high permittivity substrate has been presented and analyzed completely. A design methodology was developed and investigated based on employing a capacitive PRS on a high permittivity substrate for the first time. Then, a leaky-wave analysis was presented based on the proposed ECM and full-wave simulation to support the theory.

It has been shown that the propagation of a Q-TEM mode in a 2DLWA with a capacitive PRS, implemented on a high permittivity substrate, leads to a high-gain, high-efficient, compact, and low-profile antenna. Due to wave reflections at truncated edges of the limited-extend PRS on a high permittivity substrate, the aperture efficiency was improved up to 15% compared to the developed conventional counterpart with a capacitive PRS.

We believe that our proposed 2DLWA, together with the methodology outlined, sheds light on the realization of a high-gain and high-efficient antenna for emerging highly integrated ARoF-based systems.

References

[1] H. Chi, C. Wang, and J. Yao, "Photonic generation of wideband chirped microwave waveforms," *IEEE J. Microw.*, vol. 1, no. 3, pp. 787–803, Jul. 2021.

[2] D. Marpaung, J. Yao, and J. Capmany, "Integrated microwave photonics," *Nature Photon.*, vol. 13, no. 2, pp. 80–90, 2019.

[3] K. Zeb *et al.*, "InAs/InP quantum dash buried heterostructure mode-locked laser for high capacity fiber-wireless integrated 5G new radio fronthaul systems," *Opt. Exp.*, vol. 29, no. 11, p. 16164, May 2021.

[4] A. Hosseini, F. Capolino, and F. De Flaviis, "Gain enhancement of a V-band antenna using a Fabry–Pérot cavity with a self-sustained all-metal cap with FSS," *IEEE Trans. Antennas Propag.*, vol. 63, no. 3, pp. 909–921, Mar. 2015.

[5] S. N. Nallandhigal, P. Burasa, and K. Wu, "Deep integration and topological cohabitation of active circuits and antennas for power amplification and radiation in standard CMOS," *IEEE Trans. Microw. Theory Techn.*, vol. 68, no. 10, pp. 4405–4423, Oct. 2020.

[6] F. Liu, J. Guo, L. Zhao, G.-L. Huang, Y. Li, and Y. Yin, "Dual-band metasurface-based decoupling method for two closely packed dual-band antennas," *IEEE Trans. Antennas Propag.*, vol. 68, no. 1, pp. 552–557, Jan. 2020.

[7] X. Shen, Y. Liu, L. Zhao, G.-L. Huang, X. Shi, and Q. Huang, "A miniaturized microstrip antenna array at 5G millimeter-wave band," *IEEE Antennas Wireless Propag. Lett.*, vol. 18, no. 8, pp. 1671–1675, Aug. 2019.

[8] S. Zhu, H. Liu, Z. Chen, and P. Wen, "A compact gain-enhanced Vivaldi antenna array with suppressed mutual coupling for 5G mmWave application," *IEEE Antennas Wireless Propag. Lett.*, vol. 17, no. 5, pp. 776–779, Mar. 2018.

[9] A. R. Vaidya, R. K. Gupta, S. K. Mishra, and J. Mukherjee, "High-gain low side lobe level Fabry Perot cavity antenna with feed patch array," *Prog. Electromagn. Res. C*, vol. 28, pp. 223–238, 2012.

[10] D. R. Jackson, A. A. Oliner, and A. Ip, "Leaky-wave propagation and radiation for a narrow-beam multiple-layer dielectric structure," *IEEE Trans. Antennas Propag.*, vol. 41, no. 3, pp. 344–348, Mar. 1993.

[11] T. K. Nguyen and I. Park, "Design of a substrate-integrated Fabry–Pérot cavity antenna for K-band applications," *Int. J. Antennas Propag.*, pp. 1–12, vol. 2015, Jan. 2015, Art. No. 373801.

[12] H. Ostner, J. Detlerfsen, and D. R. Jackson, "Radiation from one-dimensional dielectric leaky-wave antennas," *IEEE Trans. Antennas Propag.*, vol. 43, no. 4, pp. 331–339, Apr. 1995.

[13] H. Yang and N. Alexopoulos, "Gain enhancement methods for printed circuit antennas through multiple superstrates," *IEEE Trans. Antennas Propag.*, vol. AP-35, no. 7, pp. 860–863, Jul. 1987.

[14] T. Zhao, D. R. Jackson, J. T. Williams, and A. A. Oliner, "General formulas for a 2D leaky-wave antenna," in *IEEE Antennas Propag. Soc. Int. Symp. Dig., USNC/CNC/URSI North Amer. Radio Sci. Meeting*, Nov. 2003, vol. 2, no. 11, pp. 1134–1137.

[15] W. Fuscaldo, "Rigorous evaluation of losses in uniform leaky-wave antennas," *IEEE Trans. Antennas Propag.*, vol. 68, no. 2, pp. 643–655, Feb. 2020.

[16] T. Zhao, D. R. Jackson, J. T. Williams, and A. A. Oliner, "Simple CAD model for a dielectric leaky-wave antenna," *IEEE Antennas Wireless Propag. Lett.*, vol. 3, pp. 243–245, 2004.

[17] X. Liu, Z. Yan, E. Wang, T. Zhang, and F. Fan, "Magnetoelectric dipole-fed Fabry–Perot antenna with wideband RCS reduction based on multilayer metasurface," *IEEE Antennas Wireless Propag. Lett.*, vol. 20, no. 7, pp. 1342–1346, Jul. 2021.

[18] G. Lovat, P. Burghignoli, and D. R. Jackson, "Fundamental properties and optimization of broadside radiation from uniform leaky-wave antennas," *IEEE Trans. Antennas Propag.*, vol. 54, no. 5, pp. 1442–1452, May 2006.

[19] Q.-Y. Guo, Q. W. Lin, and H. Wong, "A high gain millimeter-wave circularly polarized Fabry–Pérot antenna using PRS-integrated polarizer," *IEEE Trans. Antennas Propag.*, vol. 69, no. 2, pp. 1179–1183, Feb. 2021.

[20] A. Pirhadi, M. Hakkak, F. Keshmiri, and R. K. Baee, "Design of compact dual band high directive electromagnetic bandgap (EBG) resonator antenna using artificial magnetic conductor," *IEEE Trans. Antennas Propag.*, vol. 55, no. 6, pp. 1682–1690, Jun. 2007.

[21] G. Lovat, P. Burghignoli, F. Capolino, D. R. Jackson, and D. R. Wilton, "High-gain omnidirectional radiation patterns from a metal strip grating leaky-wave antenna," in *Proc. IEEE Antennas Propag. Soc. Int. Symp.*, Jun. 2007, pp. 5797–5800.

[22] S. A. Hosseini, F. Capolino, and F. De Flaviis, "Design of a single-feed 60 GHz planar metallic Fabry–Pérot cavity antenna with 20 dB gain," in *Proc. IEEE Int. Workshop Antenna Technol.*, Mar. 2009, pp. 1–4.

[23] A. Foroozesh and L. Shafai, "Investigation into the effects of the patch-type FSS superstrate on the high-gain cavity resonance antenna design," *IEEE Trans. Antennas Propag.*, vol. 58, no. 2, pp. 258–270, Feb. 2010.

[24] S. Kabiri, E. Kornaros, and F. D. Flaviss, "Wideband circular polarized Fabry–Pérot cavity antennas for V-band indoor point-to-point communications," *Electromagn.*, vol. 39, no. 3, pp. 198–216, 2019.

[25] P. Burghignoli, G. Lovat, F. Capolino, D. R. Jackson, and D. R. Wilton, "Highly polarized, directive radiation from a Fabry–Pérot cavity leaky-wave antenna based on a metal strip grating," *IEEE Trans. Antennas Propag.*, vol. 58, no. 12, pp. 3873–3883, Dec. 2010.

[26] H. Attia, M. L. Abdelghani, and T. A. Denidni, "Wideband and high-gain millimeter-wave antenna based on FSS Fabry–Pérot cavity," *IEEE Trans. Antennas Propag.*, vol. 65, no. 10, pp. 5589–5594, Oct. 2017.

[27] D. R. Jackson *et al.*, "The fundamental physics of directive beaming at microwave and optical frequencies and the role of leaky waves," *Proc. IEEE*, vol. 99, no. 10, pp. 1780–1805, Oct. 2011.

[28] Y.-F. Lu and Y.-C. Lin, "Design and implementation of broadband partially reflective surface antenna," in *Proc. IEEE Int. Symp. Antennas Propag. (APSURSI)*, Jul. 2011, pp. 2250–2253.

[29] Y. Ge, K. P. Esselle, and T. S. Bird, "The use of simple thin partially reflective surfaces with positive reflection phase gradients to design wideband, low-profile EBG resonator antennas," *IEEE Trans. Antennas Propag.*, vol. 60, no. 2, pp. 743–750, Feb. 2012.

[30] Q.-Y. Guo and H. Wong, "A millimeter-wave Fabry–Pérot cavity antenna using Fresnel zone plate integrated PRS," *IEEE Trans. Antennas Propag.*, vol. 68, no. 1, pp. 564–568, Jan. 2020.

[31] F. Xu and K. Wu, "Understanding leaky-wave structures: A special form of guided-wave structure," *IEEE Microw. Mag.*, vol. 14, no. 5, pp. 87–96, Jul./Aug. 2013.

[32] Y.-F. Lu and Y.-C. Lin, "A hybrid approach for finite-size Fabry–Pérot antenna design with fast and accurate estimation on directivity and aperture efficiency," *IEEE Trans. Antennas Propag.*, vol. 61, no. 11, pp. 5395–5401, Nov. 2013.

[33] C. Mateo-Segura, A. P. Feresidis, and G. Goussetis, "Bandwidth enhancement of 2-D leaky-wave antennas with double-layer periodic surfaces," *IEEE Trans. Antennas Propag.*, vol. 62, no. 2, pp. 586–593, Feb. 2014.

[34] D. R. Jackson, "Beaming of light at broadside through a subwavelength hole: Leaky wave model and open stopband effect," *Radio Sci.*, vol. 40, no. 6, pp. 1–2, 2005.

[35] S. Kabiri, S. A. Hosseini, F. Capolino, and F. De Flaviis, "Gain-bandwidth enhancement of 60 GHz single-layer Fabry–Pérot cavity antennas using sparse-array," in *Proc. IEEE Antennas Propag. Soc. Int. Symp. (APSURSI)*, Jul. 2014, pp. 739–740.

[36] T. K. Nguyen, D.-C. Park, and I. Park, "A single layer high gain Fabry–Pérot cavity antenna," in *Proc. Global Symp. Millim.-Waves (GSMM)*, May 2015, pp. 1–3.

[37] R. Xu *et al.*, "A review of broadband low-cost and high-gain low-terahertz antennas for wireless communications applications," *IEEE Access*, vol. 8, pp. 57615–57629, 2020.

[38] A. T. Almutawa, A. Hosseini, D. R. Jackson, and F. Capolino, "Leaky-wave analysis of wideband planar Fabry–Pérot cavity antennas formed by a thick PRS," *IEEE Trans. Antennas Propag.*, vol. 67, no. 8, pp. 5163–5175, Aug. 2019.

[39] F. Capolino, M. Albani, and V. Galdi, "Array thinning with periodic and aperiodic distributions in a Fabry–Pérot cavity for gain enhancement," in *Proc. IEEE Antennas Propag. Soc. Int. Symp.*, Jul. 2008, pp. 1–4.

[40] A. Goudarzi, M. M. Honari, and R. Mirzavand, "Resonant cavity antenna for 5G communication systems: A review," *Electronics*, vol. 9, no. 7, p. 1080, 2020.

[41] J. Zhan, F. Xu, S. Liu, S. Deng, L. Yang, and J. Qiang, "Frequency scanning Fabry–Pérot cavity antenna with single 2D-varying partial reflecting surface," *IET Microw., Antennas Propag.*, vol. 14, no. 11, pp. 1246–1252, 2020.

[42] S. A. Hosseini, F. Capolino, and F. D. Flaviis, "Q-band single-layer planar Fabry–Pérot cavity antenna with single integrated-feed," *Prog. Electromagn. Res. C*, vol. 52, pp. 135–144, 2014.

[43] Z. Li *et al.*, "Low-profile and wideband gain enhanced Fabry–Pérot cavity antenna using gradient PRS and AMC," *IET Microw., Antenna Propag.*, vol 14, no. 15, pp. 1952–1959, 2020.

[44] D. R. Jackson and A. A. Oliner, "A leaky-wave analysis of the high-gain printed antenna configuration," *IEEE Trans. Antennas Propag.*, vol. AP-36, no. 7, pp. 905–910, Jul. 1988.

[45] D. R. Jackson, C. Caloz, and T. Itoh, "Leaky-wave antenna," *Proc. IEEE*, vol. 100, no. 7, pp. 2194–2206, Jul. 2012.

[46] J. Lan, B. Sun, W. Yan, and M. Mi, "A beam scanning Fabry–Pérot cavity antenna for millimeter-wave applications," *Int. J. RF Microw. Comput.-Aided Eng.*, vol. 29, no. 5, 2019, Art. no. e21570.

[47] Y. Wang, A. Helmy, and G. Eleftheriades, "Ultra-wideband optical leaky-wave slot antennas," *Opt. Exp.*, vol. 19, no. 13, pp. 12392–12401, 2011.

[48] S. Campione, C. Gucle, Q. Song, O. Boyraz, and F. Capolino, "An optical leaky wave antenna with Si perturbation inside a resonator for enhanced optical control of the radiation," *Opt. Exp.*, vol. 20, no. 19, pp. 21305–21317, 2012.

[49] P. Burghignoli, G. Lovat, and D. R. Jackson, "Analysis and optimization of leaky-wave radiation at broadside from a class of 1-D periodic structures," *IEEE Trans. Antennas Propag.*, vol. 54, no. 9, pp. 2593–2604, Sep. 2006.

[50] A. Sutinjo, M. Okoniewski, and R. Johnston, "The effects of measurement distance on the broadside symmetric leaky wave antenna," *IEEE Antennas Wireless Propag. Lett.*, vol. 7, pp. 706–709, 2008.

[51] A. Sutinjo, M. Okoniewski, and R. H. Johnston, "Beam-splitting condition in a broadside symmetric leaky-wave antenna of finite length," *IEEE Antennas Wireless Propag. Lett.*, vol. 7, pp. 609–612, 2008.

[52] Y.-W. Hsu, H.-C. Lin, and Y.-C. Lin, "Modeling and PCB implementation of standing leaky-wave antennas incorporating edge reflection for broadside radiation enhancement," *IEEE Trans. Antennas Propag.*, vol. 64, no. 2, pp. 461–468, Feb. 2016.

[53] C. Guclu, S. Campione, O. Boyraz, and F. Capolino, "Concept of an optical leaky-wave antenna embedded in a Fabry–Pérot resonator," in *Proc. IEEE Antennas Propag. Soc. Int. Symp. (APSURSI)*, Jul. 2013, pp. 1328–1329.

[54] Q. Song, S. Campione, O. Boyraz, and F. Capolino, "Silicon-based optical leakywave antenna with narrow beam radiation," *Opt. Exp.*, vol. 19, no. 9, pp. 8735–8749, 2011.

[55] C. Guclu, S. Campione, O. Boyraz, and F. Capolino, "Theory of a directive optical leaky wave antenna integrated into a resonator and enhancement of radiation control," *J. Lightw. Technol.*, vol. 32, no. 9, pp. 1741–1749, May 1, 2014.

[56] S. Maci, M. Caiazzo, A. Cucini, and M. Casaletti, "A pole-zero matching method for EBG surfaces composed of a dipole FSS printed on a grounded dielectric slab," *IEEE Trans. Antennas Propag.*, vol. 53, no. 1, pp. 70–81, Jan. 2005.

[57] M. Garcia-Vigueras, F. Mesa, F. Medina, R. Rodriguez-Berral, and J. L. Gomez-Tornero, "Simplified circuit model for arrays of metallic dipoles sandwiched between dielectric slabs under arbitrary incidence," *IEEE Trans. Antennas Propag.*, vol. 60, no. 10, pp. 4637–4649, Oct. 2012, doi: 10.1109/TAP.2012.2207364.

[58] S. V. Hum and B. Du, "Equivalent circuit modeling for reflectarrays using floquet modal expansion," *IEEE Trans. Antennas Propag.*, vol. 65, no. 3, pp. 1131–1140, Mar. 2017.

[59] E. Baladi and S. V. Hum, "Equivalent circuit models for metasurface using floquet modal expansion of surface current distributions," *IEEE Trans. Antennas Propag.*, vol. 69, no. 9, pp. 5691–5703, Sep. 2021.

[60] C. Guclu, J. Sloan, S. Pan, and F. Capolino, "Direct use of the high impedance surface as an antenna without dipole on top," *IEEE Antennas Wireless Propag. Lett.*, vol. 10, pp. 1536–1539, 2011.

[61] Y. Ge, K. P. Esselle, and Y. Hao, "Design of low-profile high-gain EBG resonator antennas using a genetic algorithm," *IEEE Antennas Wireless Propag. Lett.*, vol. 6, pp. 480–483, 2007.

[62] A. A. Baba, R. M. Hashmi, and K. P. Esselle, "Achieving a large gain-bandwidth product from a compact antenna," *IEEE Trans. Antennas Propag.*, vol. 65, no. 7, pp. 3437–3446, Jul. 2017.

Amirhossein Askarian (Graduate Student Member, IEEE) received the M.S. degree (Hons.) in electrical engineering from the Amirkabir University of Technology (AUT), Tehran, Iran, in 2013. He is currently pursuing the Ph.D. degree with the École Polytechnique de Montréal, Montreal, QC, Canada.

In 2018, he joined the Poly-Grames Research Center, École Polytechnique de Montréal, as a Research Assistant. His current research interests include planar (2-D) leaky-wave antennas, active integrated antenna arrays (AiA), antenna-on-chip (AoC), and microwave and RF circuits design.

Mr. Askarian was a recipient of the Honorable Mention Award at IEEE AP-S 2020 Conference in Montreal, Canada. He currently serves as a Reviewer for *IET Microwaves, Antennas and Propagation*, and IEEE APS/URSI conference.

Jianping Yao (Fellow, IEEE) received the Ph.D. degree in electrical engineering from the Université de Toulon et du Var, Toulon, France, in 1997.

From 1998 to 2001, he was with the School of Electrical and Electronic Engineering, Nanyang Technological University (NTU), Singapore, as an Assistant Professor. In December 2001, he joined the School of Electrical Engineering and Computer Science, University of Ottawa, Ottawa, ON, Canada, as an Assistant Professor, where he was promoted to an Associate Professor in May 2003 and a Full Professor in May 2006. He was appointed the University Research Chair in microwave photonics in 2007. In June 2016, he was conferred the title of a Distinguished University Professor with the University of Ottawa. From July 2007 to June 2010 and July 2013 to June 2016, he was the Director of the Ottawa-Carleton Institute for Electrical and Computer Engineering, Ottawa, ON. He is a Distinguished University Professor and the University Research Chair in microwave photonics with the School of Electrical Engineering and Computer Science (EECS), University of Ottawa. He has authored or coauthored more than 660 research articles, including more than 380 articles in peer-reviewed journals and more than 280 articles in conference proceedings.

Prof. Yao was a member of the European Research Council Consolidator Grant Panel in 2016, 2018, and 2020, the Qualitative Evaluation Panel in 2017, and a panelist of the National Science Foundation Career Awards Panel in 2016. He also served as a committee member for a number of international conferences, such as IPC, OFC, CLEO, BGPP, and MWP. He was a recipient of the 2005 International Creative Research Award of the University of Ottawa, the 2007 George S. Glinski Award for Excellence in Research, and the Natural Sciences and Engineering Research Council of Canada Discovery Accelerator Supplements Award in 2008. He was selected to receive an inaugural OSA Outstanding Reviewer Award in 2012 and was one of the top ten reviewers of IEEE/OSA JOURNAL OF LIGHTWAVE TECHNOLOGY 2015–2016. He was an IEEE MTT-S Distinguished Microwave Lecturer from 2013 to 2015. He received the 2017–2018 Award for Excellence in Research of the University of Ottawa and the 2018 R.A. Fessenden Silver Medal from IEEE Canada. He was the Editor-in-Chief of the IEEE PHOTONICS TECHNOLOGY LETTERS from 2017 to 2021, a Topical Editor of *Optics Letters* from 2015 to 2017, an Associate Editor of *Science Bulletin* from 2016 to 2018, a Steering Committee Member of the IEEE JOURNAL OF LIGHTWAVE TECHNOLOGY from 2016 to 2021, and an Advisory Editorial Board Member of *Optics Communications* in 2014. He was a Guest Editor of a Focus Issue on Microwave Photonics in *Optics Express* in 2013, a Lead Editor of a Feature Issue on Microwave Photonics in *Photonics Research* in 2014, and a Guest Editor of the Special Issue on Microwave Photonics in the IEEE/OSA JOURNAL OF LIGHTWAVE TECHNOLOGY in 2018. He served as the Technical Committee Chair for IEEE MTT-S Microwave Photonics from 2016 to 2021 and an elected member of the Board of Governors of the IEEE Photonics Society from 2019 to 2021. He served as the chair for a number of international conferences, symposia, and workshops, including the Vice Technical Program Committee (TPC) Chair of the 2007 IEEE Topical Meeting on Microwave Photonics, the TPC Co-Chair of the 2009 and 2010 Asia-Pacific Microwave Photonics Conference, the TPC Chair of the high-speed and broadband wireless technologies subcommittee of the IEEE Radio Wireless Symposium from 2009 to 2012, the TPC Chair of the Microwave Photonics Subcommittee of the IEEE Photonics Society Annual Meeting in 2009, the TPC Chair of the 2010 IEEE Topical Meeting on Microwave Photonics, the General Co-Chair of the 2011 IEEE Topical Meeting on Microwave Photonics, the TPC Co-Chair of the 2014 IEEE Topical Meetings on Microwave Photonics, the General Co-Chair of the 2015 and 2017 IEEE Topical Meeting on Microwave Photonics, and the General Chair of the 2019 IEEE Topical Meeting on Microwave Photonics. He is a registered Professional Engineer of Ontario. He was an elected fellow of the Optica (formerly Optical Society of America) in 2010, the Canadian Academy of Engineering (CAE) in 2012, and the Royal Society of Canada (RSC) in 2018.

Zhenguo Lu (Member, IEEE) received the Ph.D. degree in physics from Sun Yat-sen University (Zhongshan University), Guangzhou, China, in 1992.

He has been an Adjunct Professor with the Department of Electrical and Computer Engineering, University of Ottawa, Ottawa, ON, Canada, and Concordia University, Montreal, QC, Canada, since 2006. From 1995 to 1997, he worked with the Terahertz Research Centre, Rensselaer Polytechnic Institute (RPI), Troy, NY, USA. He came to the

National Research Council Canada (NRC), Ottawa, as a Research Officer in October of 1997. From 2000 to 2002, he was the Director of Product Research and Development, BTI Systems Inc., Ottawa. He has re-joined NRC as a Senior Research Officer in 2002. He is a Principal Research Officer, a Team Lead of photonics devices, and a Project Leader of National Challenge Program "High Throughput and Secure Networks (HTSN)" with the Advanced Electronics and Photonics Research Centre, NRC. He is an expert in the field of photonics devices and their applications in optical coherent networks, data center networks, 5G and beyond wireless networks, and satellite communications. He has published more than 250 refereed journals and conference proceeding papers. He holds eight U.S. patents. He has given more than 40 invited talks at international conferences, universities, and industry companies.

Dr. Lu is a fellow of the Optica. He was a recipient of the Alexander von Humboldt (AvH) Research Fellowship to work with the Institute of Semiconductor Electronics, RWTH Aachen, Germany, for two years.

Ke Wu (Fellow, IEEE) received the B.Sc. degree (Hons.) in radio engineering from the Nanjing Institute of Technology (now Southeast University), Nanjing, China, in 1982, the D.E.A. degree (Hons.) in optics, optoelectronics, and microwave engineering from the Institut National Polytechnique de Grenoble (INPG), Grenoble, France, in 1984, and the Ph.D. degree (Hons.) in optics, optoelectronics, and microwave engineering from the University of Grenoble, Grenoble, in 1987.

He was the Founding Director of the Center for Radio Frequency Electronics Research of Quebec (Regroupement stratégique of FRQNT), Montreal, QC, Canada, and the Canada Research Chair of RF and Millimeter-Wave Engineering. He is currently a Professor of electrical engineering and the Industrial Research Chair in future wireless technologies with the Polytechnique Montréal (University of Montreal), Montreal, where he is the Director of the Poly-Grames Research Center. He has authored or coauthored more than 1400 referred articles and numerous books/book chapters and filed more than 50 patents. His current research interests involve substrate integrated circuits and systems, antenna arrays, field theory and joint field/circuit modeling, ultrafast interconnects, wireless power transmission and harvesting, microwave photonics, and megahertz–terahertz technologies and transceivers, including RFICs/monolithic microwave integrated circuits (MMICs) for multifunction wireless systems and biomedical applications.

Dr. Wu is a fellow of the Canadian Academy of Engineering, the Royal Society of Canada, and the German Academy of Science and Engineering. He is a member of the Electromagnetics Academy, URSI, and IEEE-Eta Kappa Nu (IEEE-HKN). He was a recipient of many awards and prizes, including the inaugural IEEE MTT-S Outstanding Young Engineer Award, the 2004 Fessenden Medal of the IEEE Canada, the 2009 Thomas W. Eadie Medal of the Royal Society of Canada, the Queen Elizabeth II Diamond Jubilee Medal in 2013, the 2013 FCCP Education Foundation Award of Merit, the 2014 IEEE MTT-S Microwave Application Award, the 2014 Marie-Victorin Prize (Prix du Quebec), the 2015 Prix d'Excellence en Recherche et Innovation of Polytechnique Montréal, the 2015 IEEE Montreal Section Gold Medal of Achievement, the 2019 IEEE MTT-S Microwave Prize, the 2021 EIC Julian C. Smith Medal, and the 2022 IEEE MTT-S Outstanding Educator Award. He has held key positions in and has served on various panels and international committees, including the chair of technical program committees, international steering committees, and international conferences/symposia. In particular, he was the General Chair of the 2012 IEEE Microwave Theory and Techniques (IEEE MTT-S) International Microwave Symposium (IMS) and the TPC Co-Chair of the 2020 IEEE International Symposium on Antennas and Propagation (APS). He has served on the editorial/review boards for many technical journals, transactions, proceedings, and letters as well as scientific encyclopedia, including editor, track editor, and guest editor. He was the Chair of the joint IEEE Montreal chapters of MTT-S/AP-S/LEOS and then the restructured IEEE MTT-S Montreal Chapter, Canada. He has served the IEEE MTT-S and Administrative Committee (AdCom) as the Chair for the IEEE MTT-S Transnational Committee, the Member and Geographic Activities (MGA) Committee, Technical Coordinating Committee (TCC), and the 2016 IEEE MTT-S President among many other AdCom functions. He is currently the Chair of the IEEE MTT-S Inter-Society Committee. He was a Distinguished Microwave Lecturer of the IEEE MTT-S from 2009 to 2011. He was the Inaugural Representative of North America as a member of the European Microwave Association (EuMA) General Assembly.